Full papers

Doppler splitting and expansion dynamics of laser-produced plasma plume under a high vacuum ambience†

Akira Kuwahara,*[a] Kenta Murakami,[a] Hideki Tomita,[a] Kayo Sawada,[b] Youichi Enokida[a]

[a]*Department of Applied Energy, Graduate School of Engineering, Nagoya University, Aichi 464-8603, Japan*

[b]*Institute of Materials and Systems for Sustainability, Nagoya University, Aichi 464-8601, Japan*

* Corresponding author: Akira Kuwahara

Furo-cho, Chikusa-ku, Nagoya, Aichi 464-8603, Japan.

Phone No: +81 52 789 5936

E-mail: akuwahara@energy.nagoya-u.ac.jp

† Electronic supplementary information (ESI) available. See DOI:xxx.

Abstract

The expansion behaviour and spectroscopic characteristics of laser ablation plumes under a high vacuum ambience ($<10^{-1}$ Pa) have not been investigated to date. For isotope identification using resonance ionisation mass spectrometry combined with laser ablation, a time-resolved spectroscopic investigation of the laser-produced plasma plume is necessary as the direction of atomic motions affects spectral features upon resonance ionisation due to multi-stage electron transitions. In this article, laser absorption spectroscopic measurements were conducted for the ablated plasma plume generated from an Al_2O_3 target using a nanosecond-pulsed laser. Our study mainly highlights that (i) Doppler splitting appeared after the plume front passed because of the formation of the contact layer and quasi-cavity in the plasma plume and the movement of atoms in the lateral direction at a high vacuum (3.0×10^{-4} Pa), and (ii) the loss of ejected atoms due to the laser-produced plasma expansion amounted to 43% at 3.0×10^{-4} Pa. Moreover, the two-dimensional contour figure that showed the Doppler splitting zone can be used to visualise atomic motions in the vertical and lateral directions, making it a useful tool for isotope analysis by resonance ionisation mass spectrometry.

Introduction

Resonance ionisation mass spectrometry (RIMS) provides high sensitivity and selectivity for a wide range of elements in which certain ions are obtained by resonance ionisation using multi-stage electron transitions and chemical separation is not required to remove mass interferents (*i.e.* isobars).[1–4] Thus, in the nuclear field, as RIMS can reduce the radiation exposure risk during pre-treatment and the generation of secondary radioactive waste, RIMS is particularly useful for radioactive isotope analysis. Actinide isotope analyses have been conducted by several research groups. Ziegler *et al.* demonstrated ultra-trace uranium isotope analysis using narrowband lasers for isotopic fingerprinting.[5] Schönenbach *et al.* developed a resonant laser secondary neutral mass spectrometer for plutonium isotope analysis.[6] Isselhardt *et al.* developed a correction model for laser-induced bias based on the measurement of the $^{235}U/^{238}U$ ratio.[7]

A high useful yield, the number of atoms detected per atom consumed, is considered for ultra-trace analysis (*e.g.* nuclear forensics and isotopic imaging with a high spatial resolution of a sample surface).[8,9] However, Goreinger *et al.* investigated the matrix effects and reported a useful yield of only 0.09% for U obtained from even the U metal, and the ejecta was dominated by UO and UO_2.[10] Moreover, the U atom signals drop due to the chemisorption of both oxygen atoms and molecules in both

ejecta and background gas and the population distribution in low-lying electronic states.[11] Although a useful yield of 38% from a U metal sample was achieved by developing a two-colour ionisation scheme that started from both the ground state $^5L_6$ and the low-lying electronic state $^5K_5$, atoms in the excited state amounted to only 17%.[12]

Laser ablation (LA) can be used to improve the useful yield as an atomisation source, which is a process where an intense laser beam interacts with a solid surface and laser-produced plasma (LPP) is formed by the transition of atoms, molecules, ions and nanoparticles into the gas phase. Currently, the LA process and LPP concern a broad range of fields, including thin film or nanoparticle production, analytical chemistry and nanofabrication.[13,14] LPP generated by pulsed lasers is transient, propagates at supersonic speeds and involves intricate interactions.

Various spectroscopic techniques have been used for LPP, including optical emission spectroscopy, laser-induced fluorescence and laser absorption spectroscopy (LAS),[15–22] which can directly visualise the behaviours of particles in LPP. Above all, LAS can access atoms and ions in relatively low energy states and provides valuable information without the need for complicated calibration processes (*e.g.* column density of particles and gas temperature) owing to the use of narrow-linewidth (<100 kHz)

tuneable lasers.[23–26] Miyabe *et al.* investigated the expansion dynamics of atoms and ions in LPP in the range of 10^1–10^3 Pa varying by He and Ar gas,[27] and Harilal *et al.* have particularly extended the target to LPP induced by a femtosecond-pulsed laser.[28,29] These studies and many applications of laser-induced breakdown spectroscopy have concentrated on moderate-to-atmospheric pressures in the range of 10^2–10^5 Pa. In contrast, in RIMS instruments, LPP is generated in a vacuum in the range of 10^{-4}–10^{-5} Pa to increase the mean free path of ions; thus, there is still a need for investigating the expansion dynamics of LPP in a vacuum and spectral features that affect RIMS directly. Indeed, many studies have been conducted on the expansion dynamics of LPP in a vacuum.[30–35] However, for instance, although the possibility of Doppler splitting in a vacuum has been suggested in the literature,[32] no report discusses the details of spectral profiles to understand the temporal and spatial characteristics of LPP expansion, considering the use of LAS as a probing tool. As the lateral motions of atoms and ions cause spectral shifts due to the Doppler effect, the characterisation of the propagation behaviour and appearance of LPP expansion from an absorption profile is essential for isotope analysis using RIMS.

In this study, we describe the LPP expansion behaviour at varying background pressures from 10^{-4} to 10^1 Pa observed by LAS using a resonance line (Al I 394.4006

nm) of an Al atom. First, the plume front propagation in the vertical and lateral directions was analysed using time-of-flight (TOF) absorption measurements. The absorption profiles behind the propagating plume front showed the Doppler splitting due to the blue and red peak shifts, and these findings indicated that atomic groups in the vertical direction almost did not exist inside the plasma plume. Significantly, the 2D (time–position) counter figure visualised the Doppler splitting zone and revealed atomic motions in the vertical and lateral directions for the pressure range used in a conventional RIMS instrument. Furthermore, path-integrated Al atomic number densities and translational temperatures evaluated from the absorption profiles were discussed from the standpoint of applicability for RIMS.

Experimental

A schematic of the experimental apparatus is depicted in Fig. 1. The second harmonic radiation from an Nd:YAG laser (GCR-190-10, Spectra-Physics, 532 nm, 17 ns) was used for LA. The laser pulse energy and repetition rate were ~30 mJ and 10 Hz, respectively. The focused spot size was ~120 μm (full width at half maximum), measured using a plane-convex lens (LA1708-YAG, Thorlabs) at the surface of an Al_2O_3 target (PCEA-50-7-2, Misumi, 96% purity) mounted in a cubic vacuum chamber, which was evacuated by a rotary pump (2010SD, ALCATEL), scroll pump

(SDM-320-TVL2, ANEST IWATA) and turbo molecular pump (TG220FVAB, Osaka Vacuum).

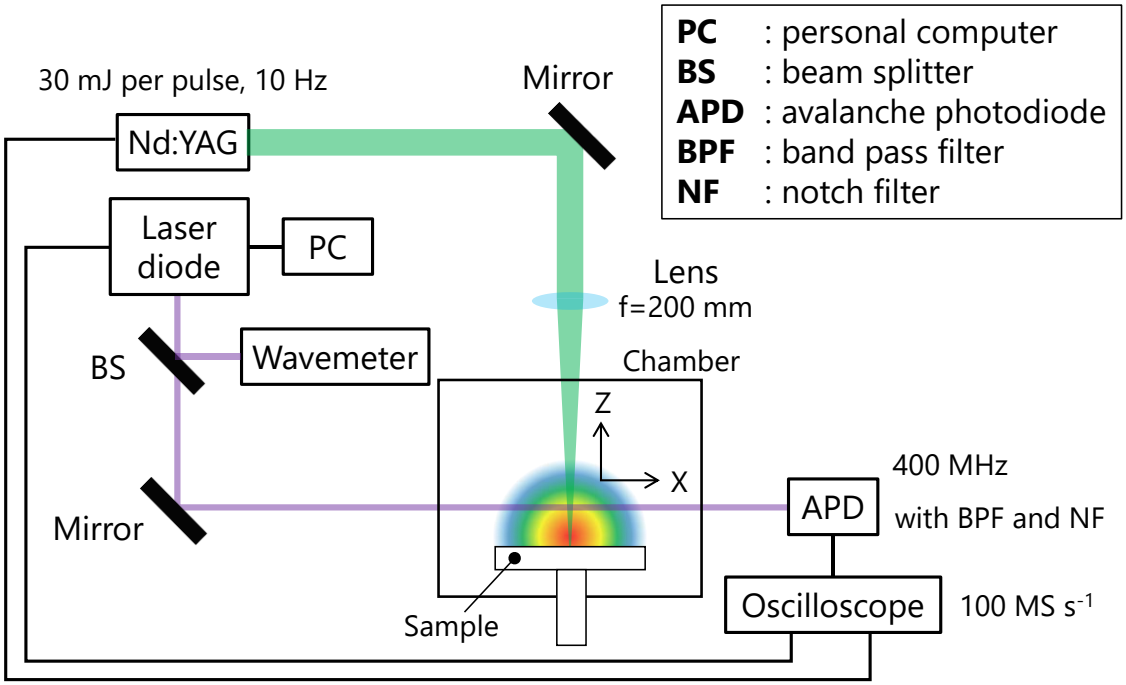

Fig. 1 Experimental apparatus of laser ablation and laser absorption spectroscopy.

LAS measurements were conducted at varying background pressures from 10^{-4} to 10^{1} Pa, where the pressures were tuned by vacuum pumps. Relative positions along the Z-axis direction between the mounted Al_2O_3 and the probe laser beam were changed by linear motion feedthrough (Ultra-Torr, Swagelok) for optical TOF measurements (Fig. 1). The collecting lens was simultaneously moved to keep the spot size at the surface.

An external cavity diode laser (DL pro, Toptica Photonics) was used as a probe laser, and its line width was approximately 100 kHz. The laser wavelength was

monitored using a wavemeter (WS6-600, HighFinesse GmbH). Absorption profiles were obtained by sweeping the wavelength of the probe laser beam with a repetition frequency of 0.98 Hz, and the width of the sweeping frequency was approximately 40 GHz. The incident laser beam intensity was fixed to a relatively low power (<100 μW) to suppress absorption saturation.

The transmitted laser beam was observed using an avalanche photodiode (APD430A2/M, Thorlabs). An optical band-pass filter (390 nm, FB390-10, Thorlabs) and a notch filter (532 nm, NF533-17, Thorlabs) were used to remove plasma emission and scattered light of pulsed laser beams. Voltage signals were recorded using a 12-bit vertical resolution recorder (DL850, Yokogawa) at a maximum sampling rate of 100 MS s^{-1}.

Results and Discussion

A strong transition of Al I 394.4006 nm ($3s^2 4s\ ^2S_{1/2} \rightarrow 3s^2 3p\ ^2P°_{1/2}$, 0–3.1427212 eV) was selected as an absorption line, which provides highly sensitive detection of aluminium atoms.[36,37] Absorption measurements were performed using fixed and scanning wavelength modes. The former was used in optical TOF measurements, and the latter was performed for obtaining an absorption profile by the accumulation of fast signals.

The ablated threshold for Al atoms was determined to be approximately 0.5 mJ, as shown in the ESI (see Fig. S1). The set pulse energy was sufficiently high for the ejection of Al atoms. In addition, as intense laser pulses produced a crater on the surface of the sample, its influence on the absorbance was preliminarily investigated. The absorbance $A(\upsilon)$ is defined as

$$A(\upsilon) = -ln\left(-I_t/I_0\,(\upsilon)\right) = k(\upsilon)L \qquad (1)$$

where $k(\upsilon)$ is the absorption coefficient, υ is the frequency and L is the absorption length. The variation in the absorbance with laser shots and a digital image of an ablated crater are shown in the ESI (see Fig. S2 and S3). As the absorbance began to decrease when laser pulses exceeded 150 shots, the number of laser shots was set to 100 for signal accumulation at the scanning wavelength mode.

Temporal profiles of the absorbance of an absorption line

TOF absorption measurements were performed using the fixed wavelength mode at the centre wavelength by simultaneously varying both the positions of the plane-convex lens and the target in the Z-axis direction. The temporal profiles of the absorbances at 10, 5.0×10^{-2}, and 3.0×10^{-4} Pa are shown in Fig. 2, where the time on the horizontal axis represents the delay time for the laser pulse. The trigger signal of the Q-switch was used as a time reference, where the jitters for the synchronisation signal of the Q-switch

and the pulse timing were ≤ 1 ns and < 0.5 ns, respectively. The absorption signals were observed even at a distance of 20 mm from the surface for all pressures, and optically thick plasma ($I_t/I_0 < 0.1$) was particularly induced at less than 10 mm (Fig. 2(a)). The arrival time of temporal profiles for Al atoms at 1 mm was approximately 150 ns at 5.0×10^{-2} and 3.0×10^{-4} Pa (Fig. 2(b) and (c)), respectively. These times show slight differences with the pressure. The propagation velocity of the plume front is discussed in the next section.

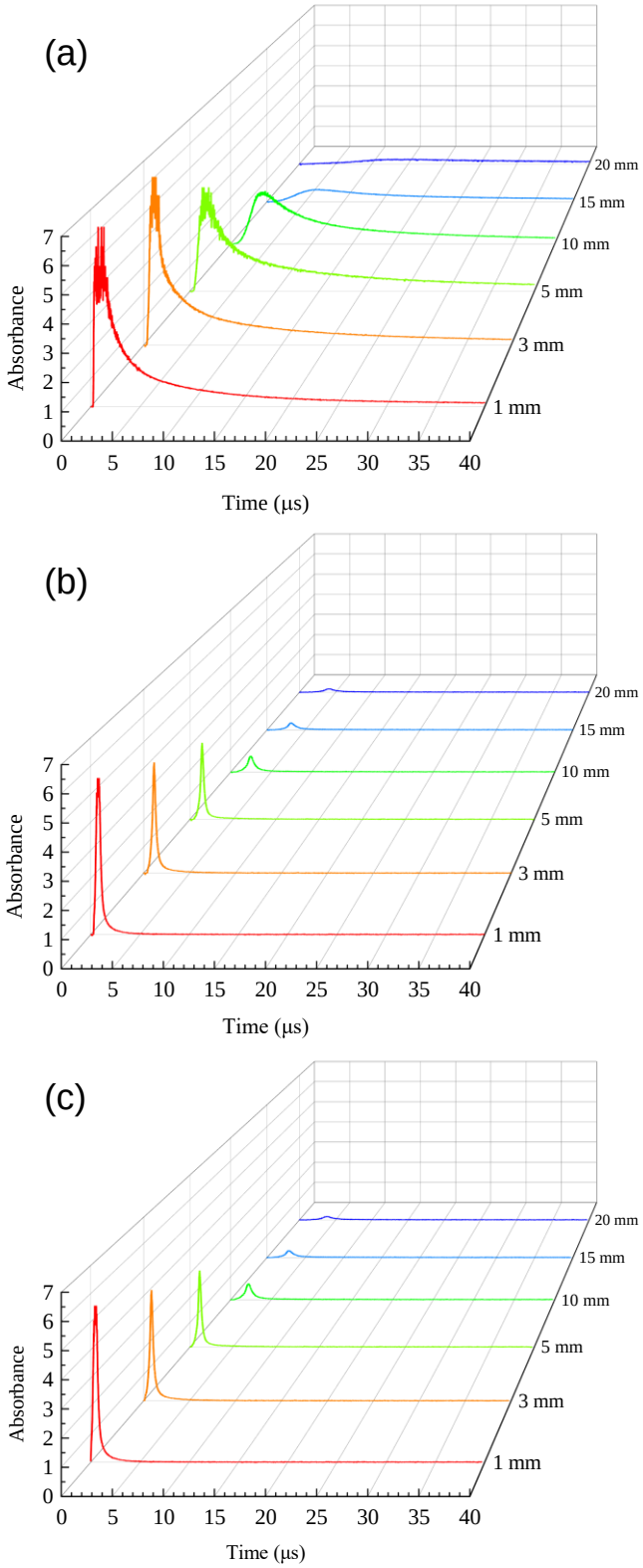

Fig. 2 Temporal profiles of absorbance through the LPP plume of (a) 10 Pa, (b) 5.0 × 10^{-2} Pa and (c) 3.0 × 10^{-4} Pa.

The temporal profiles of atoms approximately indicate a single-component distribution of atomic velocities, while the distribution of an ion has been reported to separate faster and slower groups of ions, called the double-layer effect.[31,38–41] This separation is induced by spatial charge separation in the expanding plasma. The peak at each position shifts to a later time, suggesting decay and expansion of atoms in the Z-axis direction.[32,42] The broad peak is also related to the extension of the effective absorption length with the growth of the plasma plume.

Expansion behaviour of the LPP plume in the Z-axis direction

The position–time plots are shown in Fig. 3(a). The times on the horizontal axis were evaluated from the arrival times of the absorbance peaks shown in Fig. 2, which indicates the plume front. At a medium vacuum (10 Pa), deceleration was observed because of the interactions between radicals in the plasma and residual molecules in a vacuum chamber. In contrast, at low pressures ($<10^{-1}$ Pa), the plume front behaved linearly with time, indicating free LPP expansion into the vacuum.

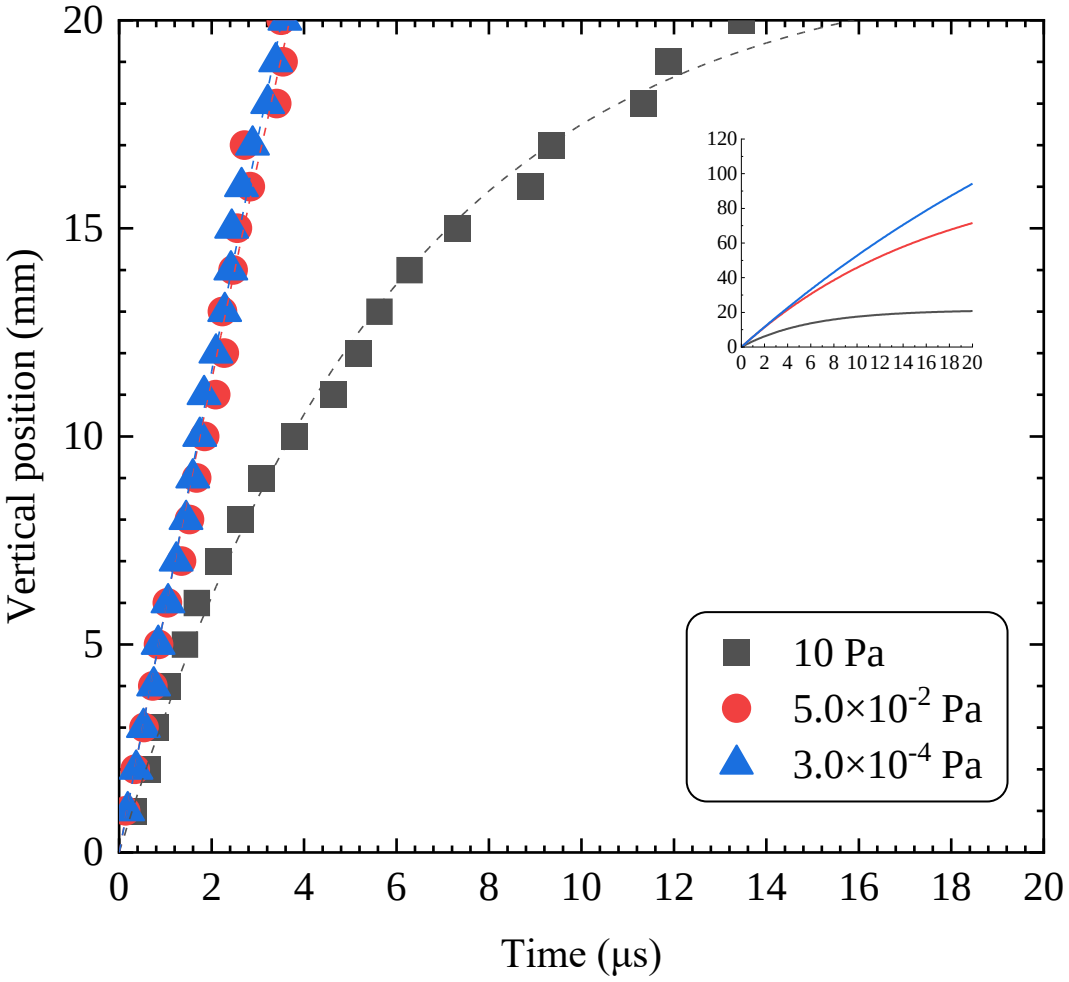

Fig. 3 Position–time plots at 10 Pa, 5.0 × 10^{-2} Pa and 3.0 × 10^{-4} Pa. The dashed lines represent the fitting of the results to the drag model.

The propagation velocity of the plume front can be evaluated from the flight time at an interval of 1 mm (Fig. 2). The propagation velocity of the plume front started slowing down at a certain position, and these analyses also confirmed the decelerations at 5.0 × 10^{-2} and 3.0 × 10^{-4} Pa on TOF measurements. In concrete terms, the plume fronts decelerated after 3, 10 and 15 mm approximately at 10, 5.0 × 10^{-2} and 3.0 × 10^{-4}

Pa, respectively.

The shock wave model and drag model have been proposed for understanding plasma dynamics.[43–51] The former can describe LPP expansion under high pressures (>1 kPa) or at its initial stage (<1 μs) under a vacuum. The latter is suitable for the later stage (>1 μs) at low pressures (<500 Pa). The LPP expansion under a high vacuum ambience can be modelled by the drag model as

$$R = R_0\{1 - \exp(-\beta t)\} \quad (2)$$

where R_0 is the stopping distance of the plume and β is the slowing coefficient. Indeed, this model predicts that LPP expansion eventually ceases due to the resistance from collisions with ambient residual molecules. The fitting of the results to the drag model is shown in Fig. 3 and Table 1. The experimental results are in good agreement with the drag model at all positions and pressures. While the stopping distance was 21.5 mm at 10 Pa, it was negligible at 5.0×10^{-2} and 3.0×10^{-4} Pa in the TOF measurement range of 1–20 mm. The distances were longer than that of the cases (≈ 6 mm) for moderate ambient pressure.[52,53]

Our results showed that the expansion behaviour of the LPP plume can be described by the drag model under a high vacuum ambience ($<10^{-1}$ Pa). In particular, for a pressure of 10^{-4} Pa, the plume front propagates at approximately 5.4×10^3 m s^{-1},

as shown in the ESI (Fig. S4), and freely expands in the ionisation region of a typical RIMS instrument without stopping. The propagation velocity under a high vacuum ambience is faster than those under higher pressures and increases with a decrease in the ambient pressure, as listed in Table 2.

Table 1 Fitting results of the drag model.

Pressure, Pa	R_0, mm	β, s^{-1}
10	21.5 ± 0.53	$1.7 \times 10^5 \pm 8.2 \times 10^3$
5.0×10^{-2}	104 ± 1.36	$5.7 \times 10^4 \pm 8.0 \times 10^2$
3.0×10^{-4}	248 ± 1.81	$2.4 \times 10^4 \pm 1.8 \times 10^2$

Table 2 Propagation velocity of the plume front.

Pressure, Pa	Velocity, m s^{-1}
10	$4.2 \times 10^3 \pm 9.1 \times 10^1$
5.0×10^{-2}	$5.1 \times 10^3 \pm 3.7 \times 10^2$
3.0×10^{-4}	$5.4 \times 10^3 \pm 6.4 \times 10^2$

Spectral features of Doppler splitting under a high vacuum ambience

Understanding the spectral characteristics of absorption profiles is vital for isotope analysis using RIMS and other applications. In this section, the absorption profiles are presented with position and time as parameters obtained by scanning the wavelength of the probe laser. The relationships between the transmittance and the Z-axis position for 3 typical transient times are shown in Fig. 4(a), (b) and (c). In addition, the absorption profiles of Al atoms are shown in Fig. 4(a), where Fig. 4(a-1)–(a-3), (b-1)–(b-3) and (c-1)–(c-3) depict the transmittance versus position for 3 typical transient times. These figures help to track the temporal variations of absorption profiles with LPP expansion. Absorption spectra at 5.0×10^{-2} Pa are presented in the ESI (Fig. S5).

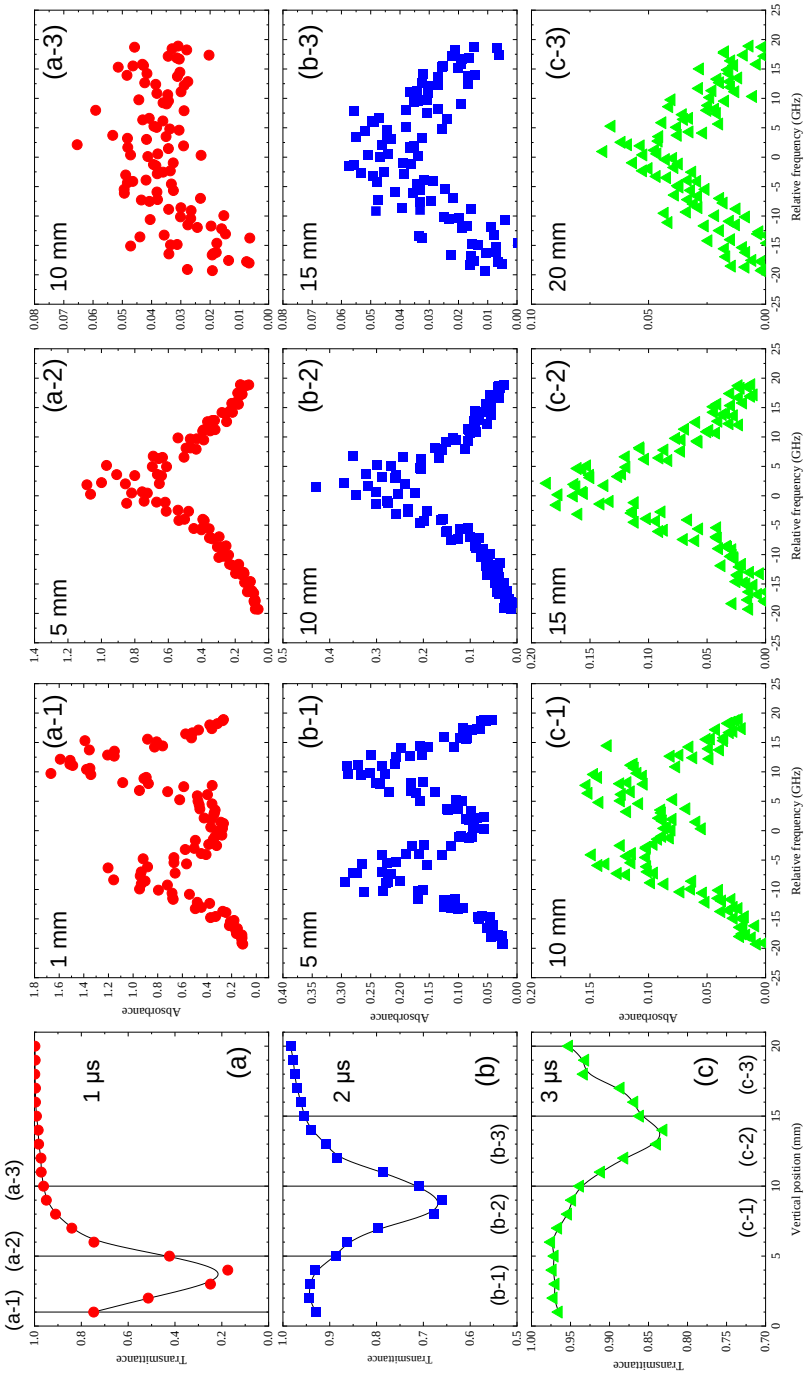

Fig. 4 Graphs showing the relationship between the transmittance and the vertical position for 3.0×10^{-4} Pa at (a) 1.0 μs, (b) 2.0 μs and (c) 3.0 μs, and absorption profiles for typical vertical positions at (a-1)–(a-3) 1.0 μs, (c-1)–(c-3) 2.0 μs and (c-1)–(c-3) 3.0 μs.

Note that aluminium has a stable ^{27}Al isotope, and an absorption line has a hyperfine structure.[36] Four transitions were observed overlapping in high-temperature plasma plumes due to Doppler broadening. The Stark broadening contributes to the Lorentz width due to charged particles at early times.[29]

At all positions, the spectral splitting of the absorption profiles from one peak into double peaks was observed for 5.0×10^{-2} Pa and 3.0×10^{-4} Pa, known as Doppler splitting. The Doppler splittings of Ce and Sr atoms were reported by Bushaw *et al.* and Miyabe *et al.* for a moderate pressure range and were associated with the presence of a contact layer.[32,42] Almost ejected particles are distributed in the boundary of the compressed front layer, defined as the contact layer, which travels in a compressed state. Man *et al.* proposed a simplified contact layer model.[49] The generated plasma plume with a hemispherical shape compresses the ambient gas in front of the shock wave. Under the presence of a contact layer, a quasi-cavity is formed inside the plasma plume. When the probe laser beam propagates after passing through the contact layer, the beam is absorbed by two atomic groups in the opposing directions of the optical axis of the probe laser beam. Atomic groups moving in the same and opposing directions of the optical axis cause blue and red wavelength shifts of the absorption line due to the Doppler effect.

For 1 μs, the absorption spectrum at 1 mm had double peaks (Fig. 4(a-1)) and the ones at 5 mm and 10 mm had one peak (Fig. 4(a-2) and (a-3)), where the plume front was near 3 mm, as shown in Fig. 4(a). For 2 μs, the plume front nearly reached 10 mm, and the Doppler splitting appeared in the absorption spectrum at 5 mm (Fig. 4(b-1)). The relationship between the spectral structure and the plume front position was similar for 3 μs (Fig. 4(c-1)–(c-3)). The Doppler components were fitted to two Gaussian functions (Fig. S7). The obtained spectra can be well described by the atomic distributions of two groups that move in the X-axis direction, while the atomic group moving in the Z-axis direction is negligible. These results indicate the formation of a contact layer and a quasi-cavity in the plasma plume at 3.0×10^{-4} Pa.

Absorption measurements in the pressure range of 200–1300 Pa conditioned with He gas were conducted by Bushaw *et al.* and Miyabe *et al.*, and clear Doppler splittings were observed.[32,42] In a moderated pressure range, the stopping distance is much shorter than that for high vacuum conditions; that is, the size of the LPP plume is relatively small. In that case, the plasma inside the contact layer after the peak-out has a high electron density at early times (<3 μs), and the spectral width broadens due to the Stark effect. Thus, Doppler splitting was not clearly observed for gases with relatively high ionisation potentials, except for He gas. In contrast, for high vacuum conditions ($<10^{-1}$

Pa), the Doppler splittings were observed even at the position of 20 mm. As the deceleration of the plasma plume was negligible in the observation region (1–20 mm), the appearance of the Doppler splitting was within the time window of the plasma lifetime after the plume front passed. For instance, although the transmittance at 15 mm for 5 μs decreased to several per cent, the Doppler splitting was observed.

The Doppler splitting zone for 3.0×10^{-4} Pa is shown in Fig. 5. The 2D counter figure (time–position) is remarkably helpful for isotope analysis using RIMS to particularly fine-tune the Z-axis position and the timing of laser irradiation for ionisation. The absorption profiles were obtained at the vertical positions of 1, 3, 5, 10, 15 and 20 mm and analysed at a time step of 100 ns. Afterwards, for other heights, the start and end positions of the red zone were linearly interpolated. The red zone indicates the appearance of Doppler splitting with the absorbance peak ≤ 0.05, and the circle plots are the same as those shown in Fig. 3. This contour figure visualised the Doppler splitting distributed behind the plume front. The red zone narrowed with the increase in the Z-axis position owing to the decrease in absorbance. The thickness of the contact layer can be estimated from the arrival time of the plume front and the vertical velocity by using the duration time of an absorption profile with a single peak. For instance, at the height of 1 mm, a single peak appeared for 510 ns. As a result, the thickness was

approximately 2.6–3.8 mm closer at the Z-axis position than the height of 5 mm, while the contact layer broadened to 9.4 mm at positions farther than 15 mm. The result that the Doppler splitting becomes less clear at farther positions depends on not only signal attenuation but also the extension of the contact layer.

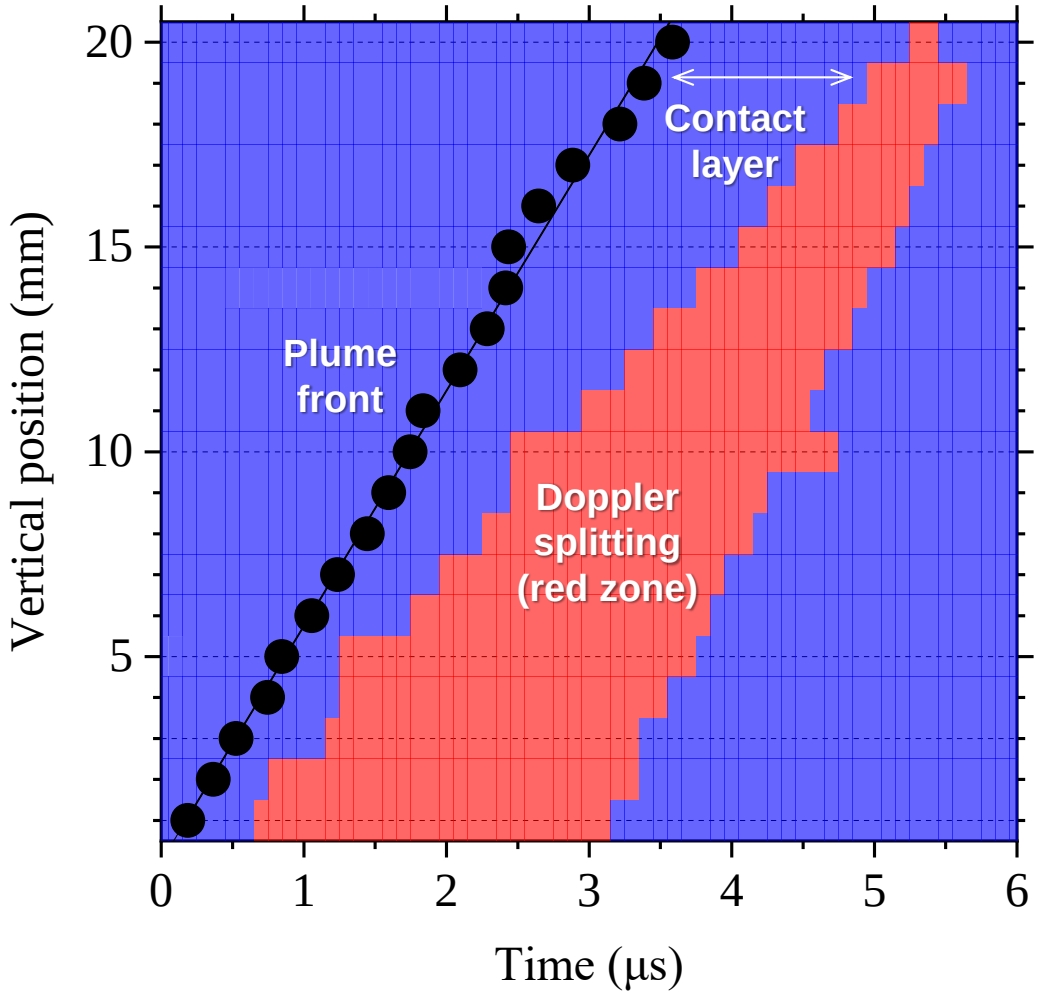

Fig. 5 2D counter figure of the appearance of Doppler splitting at 3.0×10^{-4} Pa in the red zone. Absorption profiles were obtained at the vertical positions of 1, 3, 5, 10, 15 and 20 mm, and for other heights, the start and endpoints of the red zone were linearly interpolated.

Note that the ionisation of atomic groups in different zones causes analytical errors in the accumulation of ion counting for isotope identification. The 2D counter figure provides valuable information for inferring the relationship between the excitation wavelength and isotopes, which temporally vary in the LPP plume.

Characteristics of the Doppler splitting

The expansion characteristics of atomic groups moving in the X-axis direction can be evaluated from the absorption profiles of Doppler splitting. The lateral propagation velocity V of the LPP plume is expressed as

$$V = \frac{S_{\mathrm{width}}}{2\upsilon_0} c \tag{3}$$

where S_{width} is the peak separation, υ_0 is the centre frequency and c is the speed of light. The lateral velocities at 5.0×10^{-2} and 3.0×10^{-4} Pa were estimated to be 3.3×10^3 and 3.8×10^3 m s^{-1}, respectively. These values agreed well with the speculated value obtained by extrapolation in the literature,[32] with a slight difference under a high vacuum. No clear deceleration for lateral direction was observed within the time window, where the absorption signals of Al atoms were observed. The lateral velocity was smaller than the vertical velocity, which was reported in the literature as well. Ionic groups are separated into two components (*i.e.* fast and slow groups) at a sufficiently high laser fluence, and accelerated ions move at a narrower cone angle than slow ions

and atoms.[31] This is because atomic groups moving in the vertical direction are affected by the recombination and charge transfer with faster ions in the contact layer. The lateral velocity is constant at sufficient intense pulse energy and its dependence on the lateral velocity is depicted in the ESI (Fig. S6).

Column density and translational temperature of Al atoms moving in the lateral direction

In this section, the plasma parameters of atomic groups in the lateral direction are discussed. The line-integrated column number density and translational temperature can be evaluated from the integral value and the spectral width of the absorption profile, respectively. The column number density nL can be calculated using the integration of $A(v)$ over the absorption profile as

$$nL = \frac{\int k(v)L\,dv}{3.088 \times 10^{-7}} \quad (4)$$

where n is the number density, and the denominator was calculated by the oscillator strength and the degeneracy degree. The translational temperature can be determined using the standard deviation σ of the Gaussian function according to the following equation:

$$T = \frac{M_A}{k_B}{\lambda_0}^2\sigma^2 \quad (5)$$

where M_A is the atomic mass, k_B is the Boltzmann constant and λ is the central

wavelength of the absorption line. As described above, although an absorption profile includes four transition components, for temperature evaluations, the fitting function composed of four Gauss functions was used.

The evaluated column number density for 3.0×10^{-4} Pa is shown in Fig. 6(a), and the typical fitting result is shown in the ESI (Fig. S7). The peak value of the column number density at 1 mm was approximately 4.0×10^{16} m^{-2} and is comparable to that generated using a femtosecond-pulsed laser.[29] After that, the column number density decreased to 1.4×10^{15} m^{-2} at 3 μs. In contrast, the evaluated translational temperature for 3.0×10^{-4} Pa remained relatively high, as shown in Fig. 6(b), and reached approximately 12000 K at the vertical position of 10 mm because of the suppression of atomic motion in the direction of the sample near its surface.

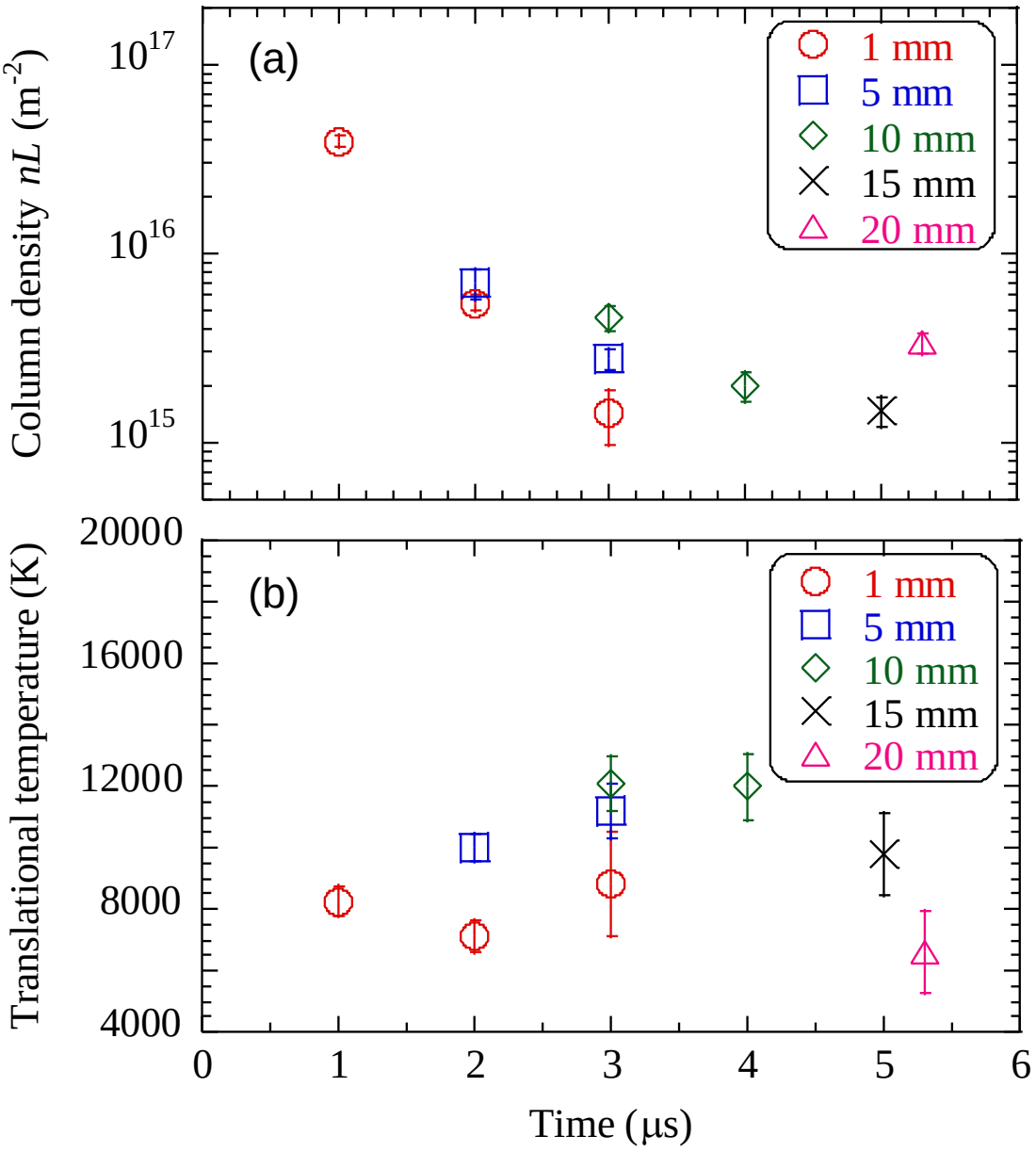

Fig. 6 (a) Column density and (b) translational temperature at 3.0×10^{-4} Pa. The error bars represent the standard deviation.

The loss due to atoms moving in the X-axis direction was evaluated, although these atoms could not reach the ionisation region. Assuming that the signal decay was

the same in the X- and Z-axis directions, the loss can be evaluated by comparing two absorption profiles with a single peak at 3 mm height and double peaks at 1 mm for 1 μs. The corresponding column number densities were 9.1×10^{16} m^{-2} and 4.0×10^{16} m^{-2}, respectively, and the loss was approximately 43%. Since atoms moving in the Z-axis direction were slightly dominant, the loss reduced the useful yield. The suppression of the loss due to LPP expansion and plasma confinement are required to apply differential pumpings, such as an orifice and supersonic nozzle.[24,25] In addition, the role of molecules in the LPP plume[54–56] and the influence of direct ionisation by LAs can provide useful information to suppress the loss and improve the analysis accuracy.

Conclusions

The LPP expansion behaviour triggered by nanosecond-pulsed LAs and spectral features under a high vacuum ambience ($< 10^{-1}$ Pa) have been investigated. Spectroscopic measurements were performed by optical TOF measurements, and the accumulation of fast signals was performed by scanning the wavelength of the probe laser at 10, 5.0×10^{-2} and 3.0×10^{-4} Pa. TOF measurements showed that atoms ejected by LA were observed to expand freely in both the X- and Z-axis directions without noticeable deceleration in the measurement range of 1–20 mm at 5.0×10^{-2} and 3.0×10^{-4} Pa. Then, the absorption profiles showed unique features ahead of and behind the

plume front. In particular, behind the plume front, the absorption profiles exhibited Doppler splitting owing to the formation of the contact layer at the plume front and the quasi-cavity in the plasma plume and the movement of atoms in the X-axis direction. The appearance of Doppler splitting and LPP expansion at a high vacuum ambience is closely related. Besides, the 2D counter figure that demonstrates the appearance of Doppler splitting not only indicates spectral features but also atomic motions in the X- and Z-axis directions, which provides temporal and spatial information about the internal structure of LPP for isotope analysis using RIMS. From the spectral analysis, we found that the loss of ejected atoms due to LPP expansion was approximately 43%. Thus, further study should address the efficient transport of ejected atoms to improve the yield and accuracy of isotope analysis.

Author Contributions

Conceptualisation and writing—original draft: A.K.; funding acquisition: A.K.; investigation: A.K., K.M.; writing—review and editing: A.K., K.M., H.T., K.S., Y.E.

Conflicts of Interest

There are no conflicts to declare.

Acknowledgements

This work was partially supported by JSPS KAKENHI Grant Number JP21H01858 and the ISIJ Research Promotion Grant. We are truly grateful to T. Shimoyama for providing technical support.

References

1) M. G. Payne, L. Deng and N. Thonnard, *Rev. Sci. Intrum.*, 1994, **65**, 2433.

2) J. S. Becker, *Spectrochim. Acta B*, 2003, **58**, 1757.

3) K. Wendt, N. Trautmann and B. A. Bushaw, *Nucl. Instr. Meth. Phys. Res. B*, 2000, **172**, 162.

4) N. Trautmann, G. Passler and K. D. Wendt, *Anal. Bioanal. Chem.*, 2004, **378**, 348.

5) S. L. Ziegler and B. A. Bushaw, *Anal. Chem.*, 2008, **80**, 6029.

6) D. Schönenbach, F. Berg, M. Breckheimer, D. Hagenlocher, P. Schönberg, R. Haas, S. Amayri and T. Reich, *Anal. Bioanal. Chem.*, 2021, **413**, 3987.

7) D. Willingham, M. R. Savina, K. B. Knight, M. J. Pellin and I. D. Hutcheon, J. Radioanal. Nucl. Chem., 2013, **296**, 407.

8) M. R. Savina, B. H. Isselhardt, A. Kucher, R. Trappitsch, B. V. King, D. Ruddle, R. Gopal and I. Hutcheon, *Anal. Chem.*, 2017, **89**, 6224.

9) T. Sakamoto, M. Morita, K. Kanenari, H. Tomita, V. Sonnenschein, K. Saito, M. Ohashi, K. Kato, T. Iguchi, T. Kawai, T. Okumura, Y. Satou and I. Wakaida, *Anal. Sci.*, 2018, **34**, 1265.

10) D. E. Goeringer, W. H. Christie and R. E. Valiga, *Anal. Chem.*, 1988, **60**, 345.

11) M. R. Savina, R. Trappitsch and B. H. Isselhardt, *Spectrochim. Acta B*, 2018, **149**,

214.

12) M. R. Savina, R. Trappitsch, A. Kucher and B. H. Isselhardt, *Anal. Chem.*, 2018, **90**, 10551.

13) C. Phipps, *Laser Ablation and its Applications*, Springer, 2007.

14) I. Strashnov, I. Izosimov, J. D. Gilmour, M. A. Denecke, J. Almiral, A. Cannavan, G. Chen, C. Dissanayake, I. Doroshenko, T. Elghali, E. Enston, B. R. Fernando, G. Kasozi, S. Kelly, M. Maqsood, S. A. Muhammad, C. Muryn, A. L. Pomerantsev, D. K. Singh, G. Smith, F. Taous, C. Webb, D. Williamson, Z. Xu, S. Yang and A. Zitek, *J. Anal. At. Spectrom.*, 2019, **34**, 1630.

15) S. S. Harilal, B. E. Brumfield, N. L. LaHaye, K. C. Hartig and M. C. Phillips, *Appl. Phys. Rev.*, 2018, **5**, 021301.

16) S. S. Harilal, N. L. LaHaye and M. C. Phillips, *Opt. Exp.*, 2017, **25**, 2312.

17) M. C. Phillips, B. E. Brumfield, N. LaHaye, S. S. Harilal, K. C. Hartig and I. Jovanovic, *Sci. Rep.*, 2017, **7**, 3784.

18) E. J. Kautz, P. J. Skrodzki, M. Burger, B. E. Bernacki, I. Jovanovic, M. C. Phillips and S. S. Harilal, *J. Anal. At. Spectrom.*, 2019, **34**, 2236.

19) P. J. Skrodzki, N. P. Shah, N. Taylor, K. C. Hartig, N. L. LaHaye, B. E. Brumfield, I. Jovanovic, M. C. Phillips, S. S. Harilal, *Spectrochim. Acta B*, 2016, **125**, 112.

20) N. L. LaHaye, S. S. Harilal, M. C. Phillips, *Spectrochim. Acta B*, 2021, **179**, 106096.

21) M. Miyabe, M. Oba, H. Iimura, K. Akaoka, A. Khumaeni, M. Kato and I. Wakaida, *Spectrochim. Acta B*, 2015, **110**, 101.

22) M. Miyabe, M. Oba, K. Jung, H. Iimura, K. Akaoka, M. Kato, H.Otobe, A. Khumaeni, I. Wakaida, *Spectrochim. Acta B*, 2017, **134**, 42.

23) A. Kuwahara, Y. Aiba, T. Nankawa and M. Matsui, *J. Anal. At. Spectrom.*, 2018, **33**, 893.

24) A. Kuwahara, Y. Aiba, S. Yamasaki, T. Nankawa and M. Matsui, *J. Anal. At. Spectrom.*, 2018, **33**, 1150.

25) A. Kuwahara, Y. Aiba and M. Matsui, *ACS Omega*, 2021, **6**, 11750.

26) V. Lebedev, J. H. Bartlett and A. Castro, *J. Anal. At. Spectrom.*, 2018, **33**, 1862.

27) M. Miyabe, M. Oba, H. Iimura, K. Akaoka, Y. Maruyama and I. Wakaida, *Appl. Phys. A*, 2010, **101**, 65.

28) B. Verhoff, S. S. Harilal, J. R. Freeman, P. K. Diwakar and A. Hassanein, *J. Appl. Phys.*, 2012, **112**, 093303.

29) S. S. Harilal, E. J. Kautz and M. C. Phillips, *Phys. Rev. E*, 2021, **103**, 013213.

30) J. R. Freeman, S. S. Harilal, P. K. Diwakar, B. Verhoff and A. Hassanein,

Spectrochim. Acta B, 2013, **87**, 43.

31) N. M. Bulgakova, A. V. Bulgakov and O. F. Bobrenok, *Phys. Rev. E*, 2000, **62**, 5624.

32) M. Miyabe, M. Oba, H. Iimura, K. Akaoka, Y. Maruyama, H. Ohba, M. Tampo and I. Wakaida, *J. Appl. Phys.*, 2012, **112**, 123303.

33) M. Ribière and B. Chéron, *Spectrochim. Acta B*, 2010, **65**, 524.

34) A. Neogi, E. T. Kennedy1, J. Mosnier, P. van Kampen, J. Costello, C. McGuinness and G O'Sullivan, *J. Phys. B: At. Mol. Opt. Phys.*, 2001, **34**, L651.

35) L. Nagli, M. Gaft and I. Gornushkin, *Appl. Opt.*, 2012, **51**, B201.

36) H. Scheibner, St. Franke, S. Solyman, J. F. Behnke, C. Wilke and A. Dinklage, *Rev. Sci. Instrum.*, 2002, **73**, 378.

37) M.Wolter, H. T. Do, H. Steffen and R. Hippler, *J. Phys. D: Appl. Phys.*, 2005, **38**, 2390.

38) M. Skočić, D. Dojić and S. Bukvić, *J. Quant. Spectrosc. Radiat. Transf.*, 2019, **227**, 57.

39) S. S. Harilal, C. V. Bindhu, M. S. Tillack, F. Najmabadi and A. C. Gaeris, *J. Appl. D*, 2002, **35**, 2935.

40) C. Focsa, S. Gurlui, P. Nica, M. Agop and M. Ziskind, *Appl. Surf. Sci.*, 2017, **424**,

299.

41) K. Yahiaoui, and S. M. Aberkane, *Spectrochim. Acta B*, 2021, **180**, 106197.

42) B. A. Bushaw and M. L. Alexander, *Appl. Surf. Sci.*, 1998, **127**, 935.

43) K. Yahiaoui, S. Abdelli-Messaci, S. Messaoud-Aberkane, T. Kerdja and H. Kellou, *Spectrochim. Acta B*, 2014, **93**, 20.

44) K. Yahiaoui, S. Abdelli-Messaci, S.M. Aberkane, M. Siad and A. Kellou, *Appl. Phys. A*, 2017, **123**, 464.

45) S. S. Harilal, C. V. Bindhu, M. S. Tillack, F. Najmabadi and A. C. Gaeris, *J. Appl. Phys.*, 2003, **93**, 2380.

46) A. K. Sharma and R. K. Thareja, *Appl. Phys. Lett.*, 2004, **84**, 4490.

47) D. B. Geohegan, *Thin Solid Films*, 1992, **220**, 138.

48) S. S. Harilal, G. V. Miloshevsky, P. K. Diwakar, N. L. LaHaye and A. Hassanein, *Phys. Plasmas*, 2012, **19**, 083504.

49) B. Y. Man, X. T. Wang and A. H. Liu, *J. Appl. Phys.*, 1998, **83**, 3509.

50) X. Zeng, X. L. Mao, R. Greif and R. E. Russo, *Appl. Phys. A*, 2005, **80**, 237.

51) A. E. Hussein, P. K. Diwakar, S. S. Harilal and A. Hassanein, *J. Appl. Phys.*, 2013, **113**, 143305.

52) S. S. Harilal, E. J. Kautz and M. C. Phillips, *J. Appl. Phys.*, 2022, **131**, 063101.

53) M. G. Tarallo, G. Z. Iwata and T. Zelevinsky, *Phys. Rev. A*, 2016, **93**, 032509.

54) D. G. Weisz, J. C. Crowhurst, W. J. Siekhaus, T. P. Rose, B. Koroglu, H. B. Radousky, J. M. Zaug, M. R. Armstrong, B. H. Isselhardt, M. R. Savina, M. Azer, M. S. Finko and D. Curreli, *Appl. Phys. Lett.*, 2017, **111**, 034101.

55) E. J. Kautz, P. J. Skrodzki, M. Burger, B. E. Bernacki, I. Jovanovic, M. C. Phillips and S. S. Harilal, *J. Anal. At. Spectrom.*, 2019, **34**, 2236.

56) S. S. Harilal, B. E. Brumfield, B. D. Cannon and M. C. Phillips, *Anal. Chem.*, 2016, **88**, 2296.